Journal of Alloys and Compounds 509 (2011) 9472–9478

Contents lists available at ScienceDirect

Journal of Alloys and Compounds

journal homepage: www.elsevier.com/locate/jallcom

A study of the synthesis of bismuth tellurium selenide nanocompounds and procedures for improving their thermoelectric performance

Cham Kim[a,b], Dong Hwan Kim[a], Jong Sook Kim[a], Yoon Soo Han[c], Jong Shik Chung[b], Hoyoung Kim[a,*]

[a] Daegu Gyeongbuk Institute of Science and Technology (DGIST), 50-1 Sang-ri, Hyeonpung-myeon, Dalseong-gun, Daegu 711-873, Republic of Korea
[b] Department of Chemical Engineering, Pohang University of Science and Technology (POSTECH), San 31 Hyoja-dong, Pohang 790-784, Republic of Korea
[c] Department of Advanced Energy Material Science and Engineering, Catholic University of Daegu, 330, Geumrak 1-ri, Hayang-eup, Gyeongsan 712-702, Republic of Korea

ARTICLE INFO

Article history:
Received 21 May 2011
Received in revised form 12 July 2011
Accepted 14 July 2011
Available online 23 July 2011

Keywords:
Thermoelectrics
ZT
Chemical synthesis
Nanocompound
$Bi_2Te_ySe_{3-y}$

ABSTRACT

A bismuth tellurium selenide ($Bi_2Te_ySe_{3-y}$) nanocompound for thermoelectric applications was successfully prepared via a water-based chemical reaction in an atmospheric environment. The compound was less that ca. 100 nm in size, with a crystalline structure corresponding to the rhombohedral $Bi_2Te_{2.7}Se_{0.3}$. We sintered the compound via a spark plasma sintering process under the designated sintering conditions and measured the transport properties (i.e., thermal conductivity, resistivity, Seebeck coefficient). The resulting specimens consisted of nanosized grains exhibiting a remarkably low thermal conductivity. Subsequently, we endeavored to improve the other transport properties by adjusting the carrier density of the compound and derived the overall thermoelectric performance by the figure of merit (ZT).

1. Introduction

Thermoelectric (TE) materials have been intensively researched because of their attractive applications, such as waste heat-to-electricity conversion and solid-state cooling [1–7]. In this field, one of the main topics of research has been the improvement of the performance of TE materials (n- and p-type semiconductors) to increase the efficiency of TE devices. The comprehensive performance of such materials is evaluated via the dimensionless figure of merit $ZT = \alpha^2\sigma T/\kappa$, where α is the Seebeck coefficient, σ is the electrical conductivity, T is the absolute temperature, and κ is the thermal conductivity [5–10]. Therefore, an excellent TE material should have both a high σ and a low κ, characteristics indicative of a so-called phonon-glass/electron-crystal (PGEC) [1,7–15].

With the meteoric development in nanotechnology, many groups have been trying to build low-dimensional structures to use as a type of PGEC material. Reports have shown that ZT can be enhanced in quantum dots (QD) and superlattice (SL) thin films both because of the increase in the power factor ($\alpha^2\sigma$) and the decrease in κ, which result from quantum confinement and the phonon scattering effect, respectively [13–21]. Relatively high ZT values are often exhibited in these QDs or SL structures, but the commercial use of these substances is difficult because of complicated production processes and high costs. Therefore, some groups have focused on using nanobulk structures, such as nanoparticles [22–24], nanotubes [25–27], and nanowires [28–30]. Not only do these nanostructures still exhibit the phonon scattering effect, which reduces κ, but they can also be prepared by cheaper methods.

TE materials are usually classified according to the temperatures at which they are operated. For low-temperature operations (0–250 °C), Bi_2Te_3-type semiconductors have primarily been investigated because of their favourable ZT value in this temperature range. The p-type semiconductor, bismuth antimony telluride ($Bi_xSb_{2-x}Te_3$), has a high $\alpha^2\sigma$, resulting in an excellent ZT value (normally about 1.0 at 50–150 °C) [14,31–33]. In addition, some research groups have endeavored to fabricate nanobulk $Bi_{0.5}Sb_{1.5}Te_3$ to reduce κ [34–38]. Thus, the highest ZT value, 1.4 at 100 °C has been achieved with this material [24]. P-type semiconductors have been actively investigated, but research into the n-type semiconductor, bismuth tellurium selenide ($Bi_2Te_ySe_{3-y}$), is relatively rare, likely because of its low ZT value. In addition, the study of a $Bi_2Te_ySe_{3-y}$ nanocompound for κ reduction has never been done, to the best of our knowledge. Therefore, we intended to synthesize this ternary nanocompound via a brief chemical synthetic route and to examine the effect of its nanostructure on κ. Moreover, we attempted to adjust some of the parameters of the preparation process, which caused large variations in the carrier density, the electrical resistivity, and the Seebeck coefficient. The whole process was optimized by choosing the pre-

* Corresponding author. Tel.: +82 53 785 3600; fax: +82 53 785 3439.
E-mail address: hoykim@dgist.ac.kr (H. Kim).

0925-8388/$ – see front matter © 2011 Elsevier B.V. All rights reserved.
doi:10.1016/j.jallcom.2011.07.040

dominant physical and transport properties that resulted in ZT enhancement.

2. Experimental details

2.1. Chemicals

Bismuth(III) nitrate ($Bi(NO_3)_3$, Kojundo chemical, 99.99%) and elemental tellurium/selenium powder (Te/Se, Kojundo chemical, 99.999%, 45 μm) were employed as precursors. Ascorbic acid ($C_6H_8O_6$, Junsei Chemicals, 99%) and ethylenediaminetetraacetic acid (EDTA: $C_{10}H_{16}N_2O_8$, Junsei Chemicals, 99.4%) were used to dissolve the bismuth precursor and to stabilize it in deionized water, respectively. Sodium borohydride ($NaBH_4$, Samchun, 99%) was chosen to reduce the Te and Se powders. All chemicals were used without any further purification.

2.2. Sample preparation

The sample preparation was based on a procedure described elsewhere [39]. $Bi(NO_3)_3$ was mixed with deionized water, and the ascorbic acid and EDTA were then added. The resulting pale yellow suspension was vigorously stirred until it reached a stable pH value (pH 1.5). Then, a solution of NaOH (5.0 M) was slowly added to the mixture to adjust the pH to 11, at which point a yellow cloudy solution was obtained that did not contain any undissolved particles. This solution became completely transparent after additional stirring for ca. 3 h (solution A). Meanwhile, Te and Se powders were placed in a three-neck round-bottom flask. The flask was purged with N_2, and then the reducing agent $NaBH_4$(aq) was added. This Te and Se mixture was heated to 100 °C with vigorous stirring. When the mixture became a transparent purple-coloured solution (reduced Te/Se solution), solution A was added at once. A black precipitate instantly appeared, and it was aged for 60 h. Then, the precipitate was filtered and rinsed thoroughly using dry ethanol and deionized water. After the precipitate was dried under vacuum at 60 °C overnight, a black powder was finally obtained. The resulting powder was sintered by spark plasma sintering (SPS; DR. Sinter, SPS-3, 20MK-IV) under a pressure of 50 MPa in an Ar atmosphere. The heating rate was 80 K min^{-1}, and the holding time at the sintering temperature was 2 min.

2.3. Characterization studies

2.3.1. Materials characterizations

Powder X-ray diffraction (XRD) patterns were collected with a D/MAX-2500 diffractometer (Rigaku) using Cu Kα radiation and a scintillation counter detector. Relevant patterns were recorded over a 2θ range of 10–80°. Field emission scanning electron microscopy (FE-SEM) micrographs were obtained using an S-4800 microscope (Hitachi) to observe the relevant morphology. Electron backscatter diffraction (EBSD) analysis was conducted with a Hitachi S-4300SE scanning electron microscope. The scan area was 30 × 30 μm, and a step size of 0.05 microns was used at an accelerating voltage of 25 kV. The EBSD sample was prepared by mechanical and vibrational polishing in an aqueous solution containing colloidal silica particles. Measurements of the chemical composition were performed on an electron probe microanalyzer (EPMA, JXA 8900R, JEOL) equipped with an energy dispersive X-ray spectrometer (EDS) and a wavelength dispersive X-ray spectrometer (WDS).

2.3.2. Thermoelectric characterizations

The electrical resistivity (ρ) and Seebeck coefficient (α) were measured simultaneously with a ZEM-3 instrument (Ulvac-Rico). The thermal conductivity (κ) is related to the thermal diffusivity (λ) by the following equation: $\kappa = \lambda C_p d$, where d and C_p denote the density and specific heat of the sample, respectively. The thermal diffusivities of the samples between 300 and 573 K were measured with a laser flash tool (LFA447, Netzsch). We adopted the C_p values of a BiTe-based thermoelectric material [40] to calculate the thermal conductivity using the above equation. The thermal conductivity is roughly determined by the sum of the carrier thermal conductivity (κ_e) and the lattice thermal conductivity (κ_L). Because the carrier thermal conductivity can be calculated by the Wiedemann–Frantz law, $\kappa_e = L_0 \sigma T$ (Lorentz number (L_0) = 2.45×10^{-8} W Ω K^{-2}), the lattice thermal conductivity can also be estimated. Consequently, the figures of merit of all samples were calculated by the following equation: $ZT = \alpha^2 \sigma T / \kappa$.

3. Results and discussion

The bismuth precursor, $Bi(NO_3)_3$ is easily hydrolyzed to form bismuth(III) hydroxide ($Bi(OH)_3$) in aqueous solutions (Eq. (1)). Therefore, we preferentially dissolved the $Bi(OH)_3$ precipitates with a reducing agent (ascorbic acid) to obtain a reactive bismuth source (i.e., Bi^{3+}). Because ascorbic acid releases protons and electrons in an aqueous solution as shown in Eq. 2 [41,42], it can possibly dissolve the $Bi(OH)_3$ precipitates and even reduce Bi^{3+} depending on pH value in the solution (Eq. (3)). The bismuth source was stabilized with a chelating agent (EDTA) so a Bi(III)-EDTA complex could be obtained (Eq. (4)).

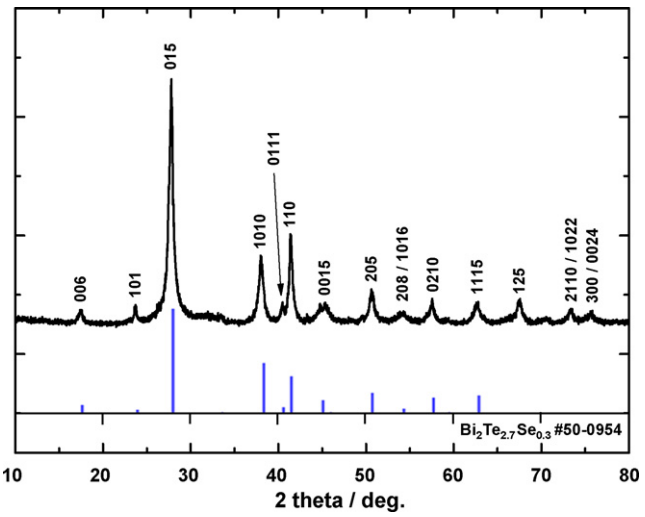

Fig. 1. A comparison between the X-ray diffraction patterns of the prepared powder sample ($Bi_2Te_ySe_{3-y}$) and the rhombohedral $Bi_2Te_{2.7}Se_{0.3}$ (JCPDS card No. 50-0954).

$$Bi(NO_3)_3\,(s) + 3H_2O\,(l) \rightarrow Bi(OH)_3\,(s)\downarrow + 3H^+ + 3NO_3^- \quad (1)$$

$$C_6H_6O_6 + 2H^+ + 2e^- \rightleftarrows C_6H_8O_6 \quad (2)$$

$$Bi(OH)_3 + H^+ \rightarrow [Bi(OH)_2]^+ + H^+ \rightarrow [Bi(OH)]^{2+} + H^+ \rightarrow Bi^{3+} \rightarrow Bi \quad (3)$$

$$Bi^{3+} + EDTA \rightarrow Bi(III)\text{-}EDTA \quad (4)$$

Te and Se powders were simultaneously reduced by $NaBH_4$, and thus Te^{2-}/Se^{2-} might be obtained (Eq. (5)). Then, the complex reacted with Te^{2-}/Se^{2-} (Eq. (6)), and the resulting powder ($Bi_2Te_ySe_{3-y}$) was examined to confirm its crystalline structure. As shown in Fig. 1, the powder sample exhibited diffraction lines corresponding to (006), (101), (015), (1010), (0111), (110), (0015), (205), (208/1016), (0210), (1115), (125), (2110/1022), and (300/0024) planes at 2θ values of 17.5°, 23.7°, 27.8°, 38.1°, 40.5°, 41.4°, 45.0°, 50.6°, 54.0°, 57.5°, 62.6°, 67.4°, 73.2°, and 75.5°, respectively, which coincide with values of the rhombohedral $Bi_2Te_{2.7}Se_{0.3}$ (JCPDS Card No. 50-0954).

$$Te/Se + BH_4^- \rightarrow Te^{2-}/Se^{2-} + H_2BO_3^- + H_2 \quad (5)$$

$$Bi(III)\text{-}EDTA + Te^{2-}/Se^{2-} \rightarrow Bi_2Te_ySe_{3-y} \quad (6)$$

The powder sample was composed of spherical nanoparticles with a uniform size (Fig. 2). The nanoparticles exhibited a very narrow particle size distribution (ca. 100 nm), possibly because EDTA controlled the reaction rate between Bi(III) ions and the reduced Te/Se by suppressing the release rate of the ions. As a result, the particle growth rate might have been depressed, and thus uniform nanoparticles could be obtained.

We sintered the powder sample by SPS to minimize the growth of the nanoparticles during the sintering process. We preferentially sintered the powder samples at both 350 °C and 400 °C because the resulting sintered specimens showed relative densities above 98% at that temperature range, while they had insufficient density or were in the liquid phase outside of that range. The two specimens were adequately treated to conduct the EBSD analysis. According to the linear-intercept method from the EBSD result, the average grain size was ca. 320 nm at 350 °C, while it increased to ca. 380 nm at 400 °C. The uniform nanoparticles (below 100 nm) of the powder

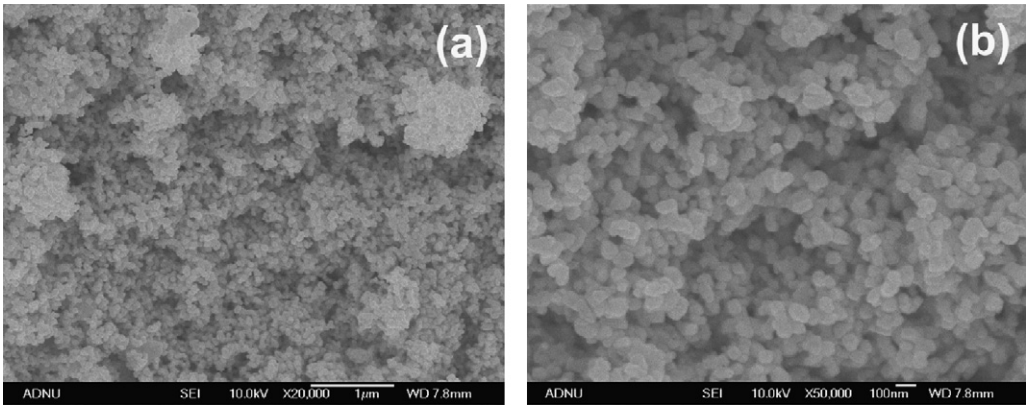

Fig. 2. SEM images of the prepared powder sample ($Bi_2Te_ySe_{3-y}$) at different magnifications.

sample seem to have grown during the sintering process, but the resulting grains did not exhibit large deviations in size depending on the sintering temperatures (Fig. 3a and c), likely because of the short sintering time of the SPS process. The specimens presented randomly oriented polycrystalline structures (as shown in Fig. 3b and d) indicating the lack of structural anisotropy in our sample. However, this result does not mean that the transport properties (thermal conductivity, electrical resistivity, Seebeck coefficient) are perfectly isotropic, regardless of whether they are measured horizontally or perpendicularly against the pressurizing direction of the SPS process. In the present study, we measured the transport properties only along the horizontal direction of the specimens.

The total thermal conductivity (κ_T) is usually determined by the sum of the lattice (κ_L) and carrier (κ_e) thermal conductivities, which are dependent on the scattering of phonons and electrons, respectively, at the grain boundaries in sintered bodies. These thermal conductivities for each specimen were properly measured and calculated as presented in Fig. 4. Because the mean free path of phonons generally ranges from 0.1 to 10 μm [43], phonons should scatter significantly in grains smaller than 10 μm, thus giving rise to the small magnitude of the lattice thermal conductivity. The specimens sintered at both the temperatures are composed of nanosized grains (Fig. 3), and as a result, phonons are expected to vigorously scatter at the grain boundaries. Hence, these specimens recorded lower lattice thermal conductivities than single crystalline bismuth tellurium selenide (sc-$Bi_2Te_{2.85}Se_{0.15}$) (Table 1). In addition, the specimens were found to have almost identical lattice thermal conductivities (Fig. 4). According to the EBSD result, elevating the sintering temperature did not cause any considerable increase in the average grain size, and thus, the phonon scattering effect

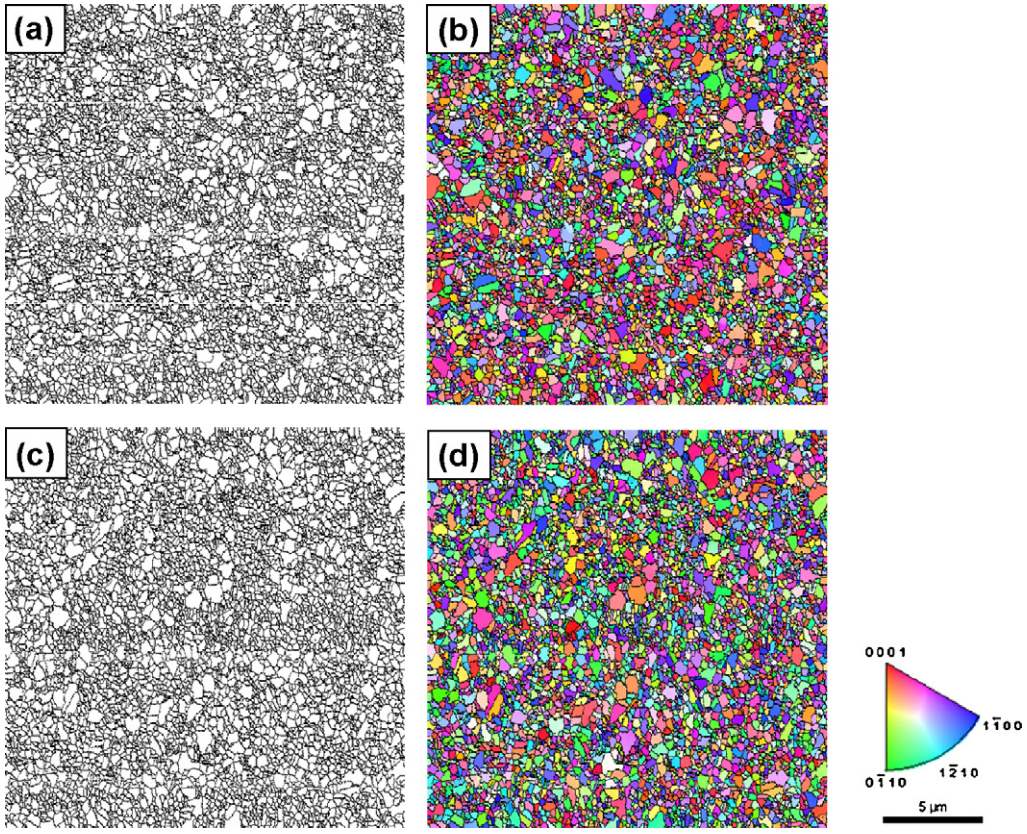

Fig. 3. Blank and inverse pole figure images for the specimens sintered at 350 °C (a and b) and 400 °C (c and d) obtained from EBSD analysis.

Table 1
Total, lattice, and carrier thermal conductivities of sc-$Bi_2Te_{2.85}Se_{0.15}$ and the specimens sintered at 350 °C and 400 °C measured at room temperature.

Sample	Total thermal conductivity/W K^{-1}	Lattice thermal conductivity/W m^{-1} K^{-1}	Carrier thermal conductivity/W m^{-1} K^{-1}	Carrier density/10^{-19} cm^{-3}
sc-$Bi_2Te_{2.85}Se_{0.15}$ [a]	1.70	0.95	0.75	5.70
Specimen (350 °C)	1.25	0.57	0.68	4.57
Specimen (400 °C)	1.73	0.58	1.15	8.01

[a] D.M. Rowe, CRC Handbook of Thermoelectrics, first ed., CRC Press, Boca Raton, 1995.

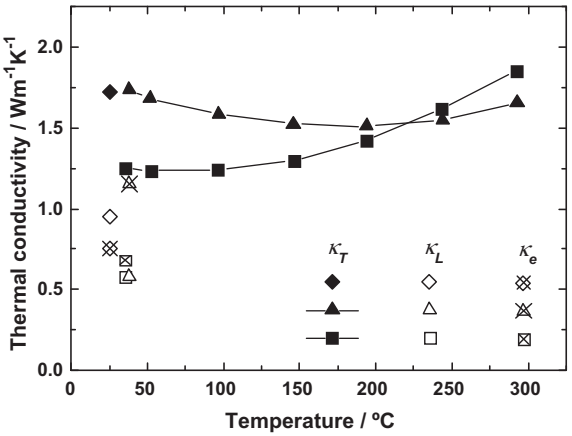

Fig. 4. Temperature dependence of the total, lattice, and carrier thermal conductivities (κ_T, κ_L, κ_e) of sc-$Bi_2Te_{2.85}Se_{0.15}$ (♦, ◊, ⊗) and the specimens sintered at 350 °C (■, □, ⊠) and 400 °C (▲, △, ⊠).

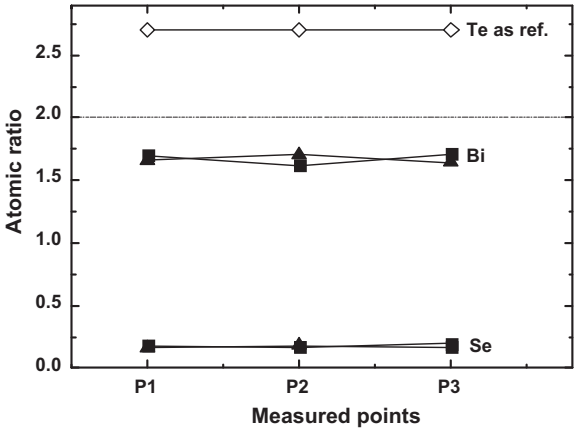

Fig. 5. Quantitative atomic compositions of the specimens sintered at 350 °C (■) and 400 °C (▲) measured by EPMA. The Te content at 2.7 (◊) was chosen as a reference to calculate the atomic ratios.

might be preserved, resulting in similar lattice terms. However, a considerable difference was found between the total thermal conductivities of the specimens because of the large gap between their carrier thermal conductivities (Table 1, Fig. 4). It is generally known that carrier thermal conductivity and resistivity are dependent on both charge carrier density and effective charge mobility. The mean free path of electrons normally ranges from 1 to 100 nm [43], and thus, the carrier thermal conductivity is expected to be mainly determined by the carrier density rather than the mobility in the nanosized grains of our specimens (average grain size ≥320 nm). As we presented in Table 1, the specimen sintered at 400 °C exhibited a higher carrier density than that sintered at 350 °C, resulting in the higher carrier thermal conductivity of the former.

The difference in the carrier density is closely related to the concentration of various intrinsic antisite defects that can possibly exist in Bi_2Te_3-type materials [44–46], such as Bi_{Te} and Te_{Bi}. According to the quantitative analysis (EPMA) of the two specimens (Fig. 5), the bismuth ratios were found to be somewhat lower than the stoichiometric bismuth ratio in the $Bi_2Te_ySe_{3-y}$ compound that we had initially attempted to produce with the bismuth precursor ($Bi(NO_3)_3$). The actual bismuth amount in the precursor seems to be lower than the theoretical bismuth amount inferred from the stoichiometry of the precursor, and this discrepancy possibly brought about the bismuth deficiencies in the specimens. Therefore, Te atoms might occupy bismuth vacancies in the crystal structure of the compound, resulting in the generation of antisite defects (Te_{Bi}). Because this phenomenon should be accelerated with an increase in sintering temperature [46], the Te_{Bi} concentration is expected to be higher in the specimen sintered at 400 °C, which results in its higher carrier density.

Fig. 6 shows the electrical resistivity and Seebeck coefficient of the sintered specimens. Because the specimen sintered at 400 °C was seen to have a higher carrier density than the specimen sintered at 350 °C (Table 1), the former showed a lower resistivity than the latter at all ranges of the measured temperatures (Fig. 6a). However, the thermoelectromotive force, i.e., the Seebeck coefficient, of the former was too small for the specimen to be used as a thermoelectric material (Fig. 6b). We assumed that the difference between the Seebeck coefficients mainly resulted from the different carrier

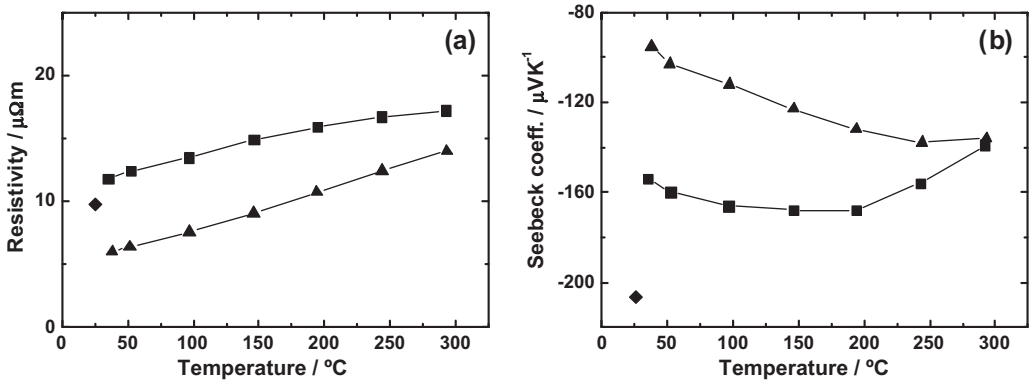

Fig. 6. Temperature dependence of the electrical resistivity (a) and Seebeck coefficient (b) of sc-$Bi_2Te_{2.85}Se_{0.15}$ (♦) and the specimens sintered at 350 °C (■) and 400 °C (▲).

densities of the specimens. On the basis of the measured values of the thermoelectric transport properties, we concluded that sintering the nanosized powder at 350 °C was preferable for obtaining favourable thermoelectric sintered bodies.

Although the specimen sintered at 350 °C had a much larger Seebeck coefficient than the another specimen, it still had a much smaller Seebeck coefficient than sc-$Bi_2Te_{2.85}Se_{0.15}$ (Fig. 6b). Because the Seebeck coefficient can significantly increase from a reduction in the carrier density, we attempted to increase the bismuth content by controlling the amount of bismuth precursor ($Bi(NO_3)_3$) used in the initial preparation process. This might be helpful to decrease the concentration of the antisite defects (Te_{Bi}), which may then possibly reduce the carrier density. Because the molecular ratio of $Bi(NO_3)_3$ was initially fixed at 2.0, we tried to adjust it to 2.1 and 2.3. According to the EPMA results shown in Fig. 7, the bismuth ratio was confirmed to rise proportionally with the increased amount of $Bi(NO_3)_3$. We present the thermoelectric transport properties of the specimens with different molar ratios of $Bi(NO_3)_3$ in Fig. 8 and Table 2. As expected, the data showed an increasing pattern for the resistivity at each temperature because of the decreasing carrier density (Fig. 8a, Table 2). The sample prepared with the largest amount of bismuth precursor (2.3) exhibited a somewhat higher resistivity than the others, but it showed the greatest Seebeck coefficient (Fig. 8b, Table 2). In addition, the maximum Seebeck coefficients for each sample were confirmed to gradually shift to low temperatures. Considering that Bi_2Te_3-type compounds are thermoelectric materials suitable for low-temperature operations, the sample that yields the maximum thermoelectromotive force at the lowest temperature (100 °C) out of all of the samples seems to be closest to the ideal stoichiometry.

The increase in the bismuth ratio also caused an additional decrease in the total thermal conductivity (Fig. 8c). The thermal conductivity gradually decreased as the bismuth content increased—a decrease of nearly 24% occurred when we increased the molar ratio of $Bi(NO_3)_3$ from 2.0 to 2.3. The carrier thermal conductivities of the samples decreased with increasing bismuth ratios at every temperature range, while the lattice thermal conductivities showed relatively small deviations (Fig. 8d). In reality, the carrier thermal conductivity decreased because of the decrease in the carrier density, as shown in Table 2, and this decrement resulted in an additional decrease in the total thermal conductivity. Consequently, we dramatically reduced the thermal conductivity—our sample with nanosized grains exhibited a lower thermal conductivity than sc-$Bi_2Te_{2.85}Se_{0.15}$ by ca. 38% at room temperature. This result is quite promising, but the sample still showed a lower Seebeck coefficient and a higher resistivity than sc-$Bi_2Te_{2.85}Se_{0.15}$, resulting in a somewhat unsatisfying ZT value, namely, a maximum

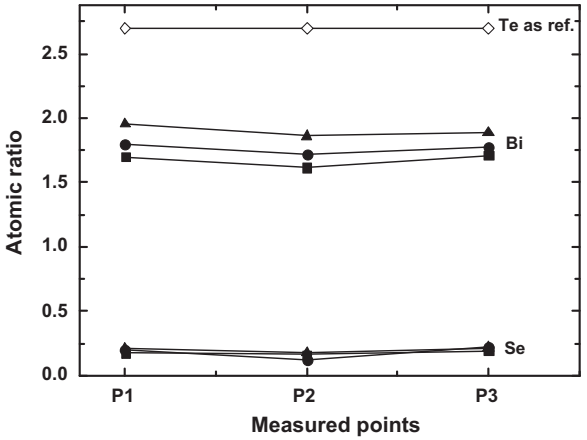

Fig. 7. Quantitative atomic compositions of the specimens prepared with different molar ratios of $Bi(NO_3)_3$: 2.0 (■), 2.1 (●), 2.3 (▲). The Te content at 2.7 (◊) was chosen as a reference to calculate the atomic ratios.

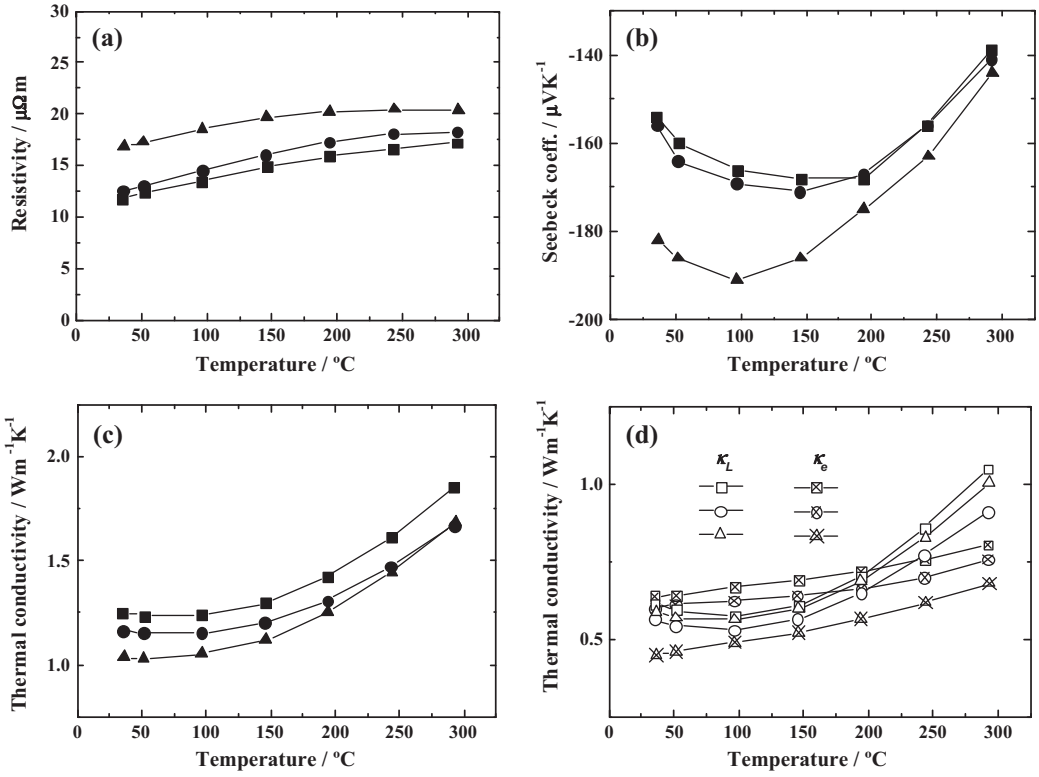

Fig. 8. Temperature dependence of the electrical resistivity (a), the Seebeck coefficient (b), the total thermal conductivity (c), and the lattice (κ_L) and carrier (κ_e) thermal conductivities (d) of the specimens prepared with the different molar ratios of $Bi(NO_3)_3$: 2.0 (■, □, ⊠), 2.1 (●, ○, ⊗), 2.3 (▲, △, ⧄).

Table 2
Variations in the transport properties of the samples prepared with different molar ratios of $Bi(NO_3)_3$ measured at room temperature.

Sample	Molar ratio of $Bi(NO_3)_3$	Carrier density/10^{-19} cm^{-3}	Resistivity/ μΩ m	Seebeck coefficient/μV K^{-1}
1	2.0	4.57	11.8	−154
2	2.1	4.11	12.6	−156
3	2.3	2.87	16.9	−182

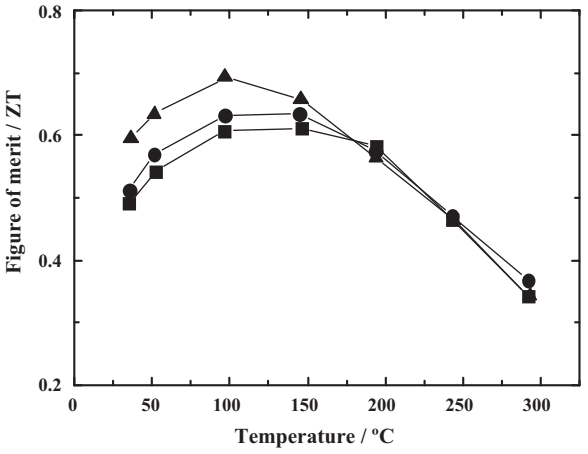

Fig. 9. Temperature dependence of the figure of merit of the specimens prepared with different molar ratios of $Bi(NO_3)_3$: 2.0 (■), 2.1 (●), 2.3 (▲).

ZT value of 0.7 at 100 °C and a worse performance of 0.6 at 25 °C (Fig. 9).

Currently, we are attempting to adjust the Se doping ratio for the further improvement of ZT with the goal of improving the Seebeck coefficient. The Fermi energy of a BiTe-type material might be set in the vicinity of the conduction band edge because of Se doping, indicating the generation of more steps in the electronic density of states (DOS). Because the Seebeck coefficient is proportional to the energy derivative of the DOS at the Fermi energy, the Seebeck coefficient can possibly be improved via the doping procedure [47,48]. The DOS of our nanosized compound might be quite different from that of conventional materials (i.e., sc-$Bi_2Te_{2.85}Se_{0.15}$), and thus the Se composition that yields an ideal Seebeck coefficient might also be different. Namely, the atomic composition must be adjusted to obtain an ideal Seebeck coefficient and further ZT enhancement.

4. Conclusions

A bismuth tellurium selenide nanocompound was successfully synthesized using a water-based chemical reaction. We sintered the compound via spark plasma sintering to preserve its nanostructure. Depending on the sintering temperatures, specimens with insufficient density or those in a liquid phase were obtained, and the transport properties (i.e., thermal conductivity, resistivity, Seebeck coefficient) varied significantly. The resulting specimen was composed of nanograins with an average size of ca. 320 nm. This specimen showed a lower lattice thermal conductivity than single-crystalline bismuth telluride (sc-$Bi_2Te_{2.85}Se_{0.15}$), which seemed to be caused by vigorous phonon scattering at the boundaries of the nanosized grains. On the other hand, the specimen exhibited a low Seebeck coefficient because of its high carrier density. Adjusting the bismuth content gave rise to large variations in the carrier density and the thermoelectric transport properties. Up to now, the overall thermoelectric performance as captured by the figure of merit (ZT) has been improved but is still unsatisfactory. Various adjustments of the atomic composition are still under investigation for further improvement of the thermoelectric properties.

Acknowledgement

This work was financially supported by the DGIST R & D Program of the Ministry of Education, Science and Technology (MoEST) of Korea (no. 11-EN-01).

References

[1] M.S. Dresselhaus, G. Chen, M.Y. Tang, R.G. Yang, H. Lee, D.Z. Wang, Z.F. Ren, J.P. Fleurial, P. Gogna, Adv. Mater. 19 (2007) 1.
[2] M.S. Dresselhaus, G. Chen, M.Y. Tang, R.G. Yang, H. Lee, D.Z. Wang, Z.F. Ren, J.P. Fleurial, P. Gogna, Mater. Res. Soc. Symp. Proc. 886 (2006), 0886-F01-01.
[3] D.F. Byrnes, B. Heshmatpour, Mater. Res. Soc. Symp. Proc. 886 (2006), 0886-F12-03.
[4] T.M. Tritt, B. Zhang, N. Gothard, J. He, X. Ji, D. Thompson, J.W. Kolis, Mater. Res. Soc. Symp. Proc. 886 (2006), 0886-F02-01.
[5] J. Sootsman, H. Kong, C. Uher, A. Downey, J.J. D'Angelo, C.-I. Wu, T. Hogan, T. Caillat, M. Kanatzidis, Mater. Res. Soc. Symp. Proc. 1044 (2008), 1044-U08-01.
[6] K.F. Hsu, S. Loo, F. Guo, W. Chen, J.S. Dyck, C. Uher, T. Hogan, E.K. Polychroniadis, M.G. Kanatzidis, Science 303 (2004) 818.
[7] X. Ji, B. Zhang, T.M. Tritt, J.W. Kolis, A. Kumbhar, J. Electron. Mater. 36 (2007) 721.
[8] T.J. Zhu, Y.Q. Liu, X.B. Zhao, Mater. Res. Bull. 43 (2008) 2.
[9] A. Rey, M. Faraldos, J.A. Casas, J.A. Zazo, A. Bahamonde, J.J. Rodríguez, Key Eng. Mater. 368–372 (2008) 550.
[10] J. Martin, G.S. Nolas, W. Zhang, L. Chen, Appl. Phys. Lett. 90 (2007) 222112.
[11] G.J. Snyder, M. Christensen, E. Nishibori, T. Caillat, B.B. Iversen, Nat. Mater. 3 (2004) 458.
[12] G.S. Nolas, J. Sharp, H.J. Goldsmid, Thermoelectrics: Basic Principles and New Materials Developments, vol. 45, Springer, Berlin, 2001.
[13] K. Kurosaki, T. Matsuda, M. Uno, S. Kobayashi, S. Yamanaka, J. Alloys Compd. 319 (2001) 271.
[14] H.J. Goldsmid, Introduction to Thermoelectricity, vol. 121, Springer, Berlin, 2009.
[15] J. Peng, J. He, P.N. Alboni, T.M. Tritt, J. Electron. Mater. 38 (2009) 981.
[16] G.S. Nolas, D.T. Morelli, T.M. Tritt, Annu. Rev. Mater. Sci. 29 (1999) 89.
[17] G. Min, D.M. Rowe, J. Mater. Sci. Lett. 18 (1999) 1305.
[18] A. Grytsiv, P. Rogl, S. Berger, C. Paul, H. Michor, E. Bauer, G. Hilscher, C. Godart, P. Knoll, M. Musso, W. Lottermoser, A. Saccone, R. Ferro, T. Roisnel, H. Noel, J. Phys.: Condens. Matter. 14 (2002) 7071.
[19] J. Tang, T. Rachi, R. Kumashiro, M.A. Avila, K. Suekuni, T. Takabatake, F.Z. Guo, K. Kobayashi, K. Akai, K. Tanigaki, Phys. Rev. B 78 (2008) 085203.
[20] R.P. Hermann, F. Grandjean, V. Keppens, W. Schweika, G.S. Nolas, D.G. Mandrus, B.C. Sales, H.M. Christen, P. Bonville, G.J. Long, Mater. Res. Soc. Symp. Proc. 886 (2005), 0886-F10-01.
[21] S. Paschen, V. Pacheco, A. Bentien, A. Sanchez, W. Carrillo-Cabrera, M. Baenitz, B.B. Iversen, Yu. Grin, F. Steglich, Physica B 328 (2003) 39.
[22] Y. Deng, X. Zhou, G. Wei, J. Liu, C.-W. Nan, S. Zhao, J. Chem. Solids 63 (2002) 2119.
[23] X. Ji, X. Zhao, Y. Zhang, B. Lu, H. Ni, Mater. Res. Soc. Symp. Proc. 793 (2004), S1.4.
[24] B. Poudel, Q. Hao, Y. Ma, Y. Lan, A. Minnich, B. Yu, X. Yan, D. Wang, A. Muto, D. Vashaee, X. Chen, J. Liu, M.S. Dresselhaus, G. Chen, Z. Ren, Science 320 (2008) 634.
[25] X.B. Zhao, X.H. Ji, Y.H. Zhang, T.J. Zhu, J.P. Tu, X.B. Zhang, Appl. Phys. Lett. 86 (2005) 062111.
[26] J. Hone, I. Ellwood, M. Muno, A. Mizel, M.L. Cohen, A. Zettl, A.G. Rinzler, R.E. Smalley, Phys. Rev. Lett. 80 (1998) 1042.
[27] Y.Q. Cao, T.J. Zhu, X.B. Zhao, J. Alloys Compd. 449 (2008) 109.
[28] J. Lu, Q. Han, X. Yang, L. Lu, X. Wang, Mater. Lett. 61 (2007) 3425.
[29] X.B. Zhao, X.H. Ji, Y.H. Zhang, B.H. Lu, J. Alloys Compd. 368 (2004) 349.
[30] T. Sun, X.B. Zhao, T.J. Zhu, J.P. Tu, Mater. Lett. 60 (2006) 2534.
[31] J.K. Lee, S.D. Park, B.S. Kim, M.W. Oh, S.H. Cho, B.K. Min, H.W. Lee, M.H. Kim, Electron. Mater. Lett. 6 (2010) 201.
[32] L.D. Hicks, T.C. Harman, X. Sun, M.S. Dresselhaus, Phys. Rev. B 53 (1996), R10-493.
[33] Z. Gu, Y. Han, F. Pan, X. Wang, D. Weng, S. Zhou, Mater. Sci. Forum 610–613 (2009) 394.
[34] Y. Zhang, G. Xu, J. Mi, F. Han, Z. Wang, C. Ge, Mater. Res. Bull. 46 (2011) 760.
[35] M.E. Anderson, S.S.N. Bharadwaya, R.E. Schaak, J. Mater. Chem. 20 (2010) 8362.

[36] Y. Zhao, C. Burda, Appl. Mater. Interfaces 1 (2009) 1259.
[37] Y. Zhao, J.S. Dyck, B.M. Hernandez, C. Burda, J. Am. Chem. Soc. 132 (2010) 4982.
[38] A. Datta, J. Paul, A. Kar, A. Patra, Z. Sun, L. Chen, J. Martin, G.S. Nolas, Cryst. Growth Des. 10 (2010) 3983.
[39] C. Kim, D.H. Kim, Y.S. Han, J.S. Chung, S. Park, S.H. Park, H. Kim, Mater. Res. Bull. 46 (2011) 407.
[40] M. Binnewies, E. Milke, Thermochemical Data of Elements and Compounds, second ed., Wiley-VCH, Weinheim, 2002.
[41] W. Songping, M. Shuyuan, Mater. Chem. Phys. 89 (2005) 423.
[42] W. Songping, Mater. Lett. 61 (2007) 1125.
[43] J.S. Blakemore, Solid State Physics, second ed., Cambridge University Press, Cambridge, 1985.
[44] J. Horák, K. Čermák, L. Koudelka, J. Phys. Chem. Solids 47 (1986) 805.
[45] Z. Starý, J. Horák, M. Stordeur, M. Stölzer, J. Phys. Chem. Solids 49 (1988) 29.
[46] N. Keawprak, Z.M. Sun, H. Hashimoto, M.W. Barsoum, J. Alloys Compd. 397 (2005) 236.
[47] N.F. Mott, E.A. Davis, Electronic Processes in Non-Crystalline Materials, second ed., Clarendon Press, Oxford, 1979.
[48] F. Salleh, H. Ikeda, J. Electron. Mater. (2010), doi:10.1007/s11664-010-1405-z.